

A Stress Self-Adaptive Bimetallic Stellar Nanosphere for High-Energy Sodium-Ion Batteries

Jun Chen, Guilai Zhang, Jun Xiao, Jiayi Li, Yang Xiao, Dingyi Zhang, Hong Gao,*
Xin Guo, Guoxiu Wang,* and Hao Liu*

Bimetallic composites exhibit great potential as anode materials in advanced energy storage systems owing to their inherent tunability, cost-effectiveness, and simultaneous achievement of high specific capacity and low reaction potential. However, simple biphasic mixing often fails to achieve satisfactory performance. Herein, an innovative stress self-adaptive bimetallic stellar nanosphere (50–200 nm) wherein bismuth (Bi) is fabricated, as a core, is seamlessly encapsulated by a tin (Sn) sheath (Sn-Bi@C). This well-integrated stellar configuration with bimetallic nature embodies the synergy between Bi and Sn, offering fortified conductivity and heightened sodium ion diffusion kinetics. Moreover, through meticulous utilization of finite element analysis simulations, a homogeneous stress distribution within the Sn-enveloped Bi, efficiently mitigating the structural strain raised from the insertion of Na⁺ ions, is uncovered. The corresponding electrode demonstrates remarkable cyclic stability, as it exhibits no capacity decay after 100 cycles at 0.1 A g⁻¹. Furthermore, it achieves an impressive 86.9% capacity retention even after an extensive 2000 cycles. When employed in a Na₃V₂(PO₄)₃ || Sn-Bi@C full cell configuration, it demonstrates exceptional capacity retention of 97.06% after 300 cycles at 1 A g⁻¹, along with a high energy density of 251.2 W h kg⁻¹.

the pursuit of high specific capacity in anode materials impose constraints on the realization of exceptional specific energy performance.^[5–6]

Bismuth-based materials, renowned for their lower reaction potential and reduced volumetric variations in comparison to their alloy counterparts, have gained significant attention as anode materials for SIBs.^[7–10] However, the gravimetric specific capacity of pure Bi (384 mA h g⁻¹) falls short of meeting the requirements for high energy density in SIBs. To address this limitation, incorporation of Bi composites has emerged as a promising strategy, leveraging the synergistic effects between Bi and other alloy-type materials to achieve satisfied specific capacity and stable cyclability concurrently. Hu et al. fabricated electrodes composed of Bi-Sb alloy/carbon nanofibers for SIBs.^[11] The lattice chemistry of the rhomboid Bi-Sb alloy was adjusted to mitigate stress variations and enhance cycling stability. The electrode exhibited a specific capacity of 233 mA h g⁻¹

after 2500 cycles at 2 A g⁻¹. Similarly, Ding et al. reported the synthesis of 1D carbon fibers with uniformly encapsulated inner BiSb_x nanoparticles (BiSb_x@C).^[12] The BiSb_x@C electrode demonstrated an 86.4% capacity retention at 0.05 A g⁻¹ after 100 cycles. Additionally, Nqobile et al. prepared bimetallic BiSn films directly on a copper collector using the electrochemical atomic

1. Introduction

Economically viable and inherently safe sodium-ion batteries (SIBs) have garnered significant attention as formidable contenders for advanced energy storage platforms.^[1–4] Nonetheless, the persistent challenges pertaining to cyclic stability and

J. Chen, G. Zhang, J. Xiao, J. Li, Y. Xiao, D. Zhang, H. Gao
Joint International Laboratory on Environmental and Energy Frontier
Materials
School of Environmental and Chemical Engineering
Shanghai University
Shanghai 200444, P. R. China
E-mail: hgao1122@shu.edu.cn

The ORCID identification number(s) for the author(s) of this article can be found under <https://doi.org/10.1002/adfm.202307959>

© 2023 The Authors. Advanced Functional Materials published by Wiley-VCH GmbH. This is an open access article under the terms of the Creative Commons Attribution-NonCommercial-NoDerivs License, which permits use and distribution in any medium, provided the original work is properly cited, the use is non-commercial and no modifications or adaptations are made.

DOI: 10.1002/adfm.202307959

X. Guo
Faculty of Materials Science and Energy Engineering/Institute of
Technology for Carbon Neutrality
Shenzhen Institute of Advanced Technology
Chinese Academy of Sciences
Shenzhen, Guangdong 518055, China
G. Wang, H. Liu
Centre for Clean Energy Technology
Faculty of Science
University of Technology Sydney
Broadway, Sydney, NSW 2007, Australia
E-mail: Guoxiu.Wang@uts.edu.au; hao.liu@uts.edu.au

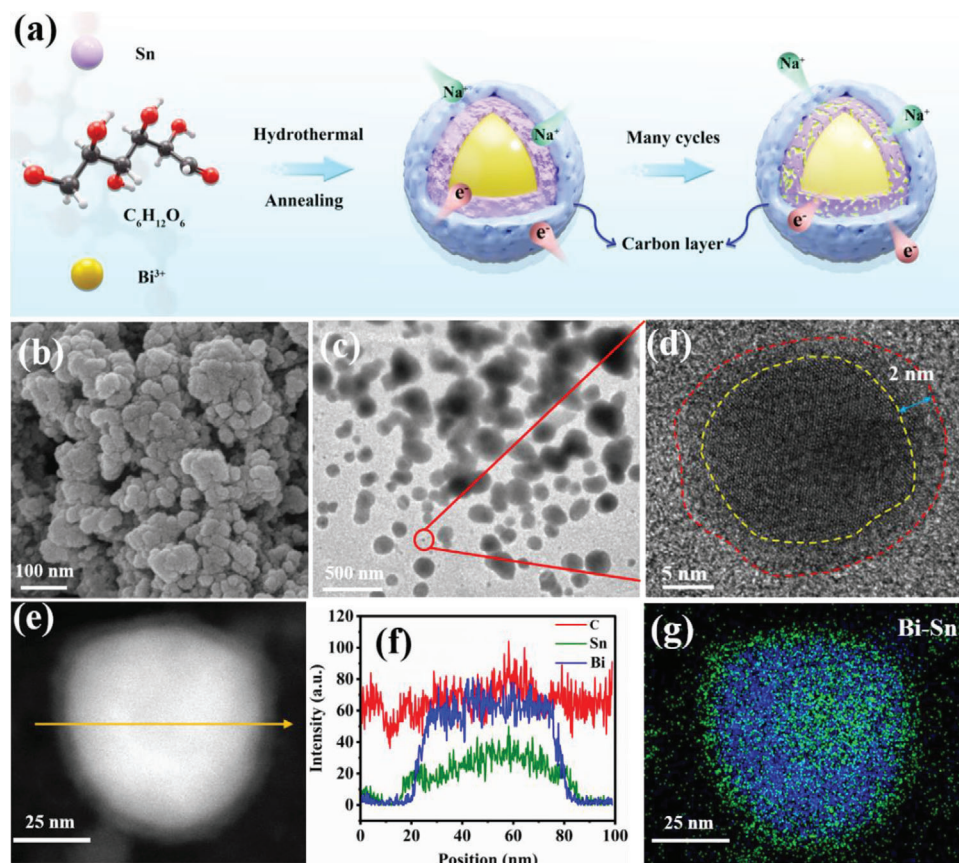


Figure 1. a) Schematic illustration of the synthetic procedure of Sn-Bi@C. b) SEM, c) TEM, and d) HR-TEM images of Sn-Bi@C. e, f) STEM image and the line-scanning profiles of Sn, Bi, and C along the orange line. g) EDX elemental mapping images of an individual Sn-Bi@C.

deposition technique. At a current density of 38.5 mA g^{-1} , an initial capacity of 341 mA h g^{-1} was achieved.

It is evident that the attainment of bimetallic composite anode materials with exceptional electrochemical properties necessitates more than mere biphasic mixing. The incorporation of distinctive structural characteristics is imperative for the development of such bimetallic composite anode materials. Building on our previous research,^[13] we have capitalized on the favorable cyclic stability of Bi metal and the notable specific capacity ($\text{Na}_{15}\text{Sn}_4$: 847 mA h g^{-1}) and low reaction potential ($\approx 0.2 \text{ V}$ vs Na^+/Na) of Sn metal^[14–16] to engineer a carbon-coated bimetallic stellar architecture, comprising Bi-centric core enveloped by the Sn sheath to construct the nanoparticle, which is further encapsulated by carbon. The well-integrated stellar configuration harnesses the synergistic effects between Bi and Sn, resulting in enhanced conductivity and accelerated sodium ion diffusion kinetics. By employing meticulous finite element analysis simulations, we have revealed a homogeneous stress distribution within the Sn-enveloped Bi structure, effectively alleviating the structural strain caused by the insertion of Na^+ ions. Therefore, the as-prepared Sn-Bi@C electrode demonstrates a specific capacity of 461 mA h g^{-1} with impressive 100% capacity retention after 100 cycles at 0.1 A g^{-1} . Meanwhile, it exhibits outstanding long-term cycling stability, retaining 86.9% of its initial capacity after 2000 cycles at 1 A g^{-1} . In the context of a $\text{Na}_3\text{V}_2(\text{PO}_4)_3 \parallel \text{Sn-Bi@C}$ full cell, a remarkable 97.06% capacity retention is achieved after

300 cycles at 1 A g^{-1} . Notably, the full cell showcases a high energy density up to $251.2 \text{ W h kg}^{-1}$, highlighting its promising practical application potential. This study presents a novel approach for regulating structural stress in bimetallic anode materials, offering valuable insights for future research in this field.

2. Result and Discussion

As shown in **Figure 1a**, the Sn-Bi@C stellar nanoparticle is prepared by facile hydrothermal reaction followed by annealing process. The meticulously integrated stellar architecture can effectively alleviate the structural expansion caused by the Na^+ ions insertion. The scanning electron microscopy (SEM) and transmission electron microscopy (TEM) images of Sn-Bi@C clearly exhibit the nanoparticle structures (50–200 nm) (Figure 1b,c). As shown in Figure 1d, the structure of Sn-Bi@C is characterized by an unusual arrangement, where a core encased into an ultrathin layer (2 nm). The scanning transmission electron microscopy (STEM) and corresponding line-scanning profiles across the Sn-Bi@C nanoparticle provide evidence of the core-shell configuration (Figure 1e,f). In addition, the unique structure of Sn-Bi@C is further confirmed by the energy dispersive X-ray (EDX) elemental mapping. As clearly shown in Figure 1g; and Figure S1 (Supporting Information), the encapsulated Bi core (blue) is surrounded by the outer Sn shell (green). This special structure maybe caused by the difference in melting points between Sn

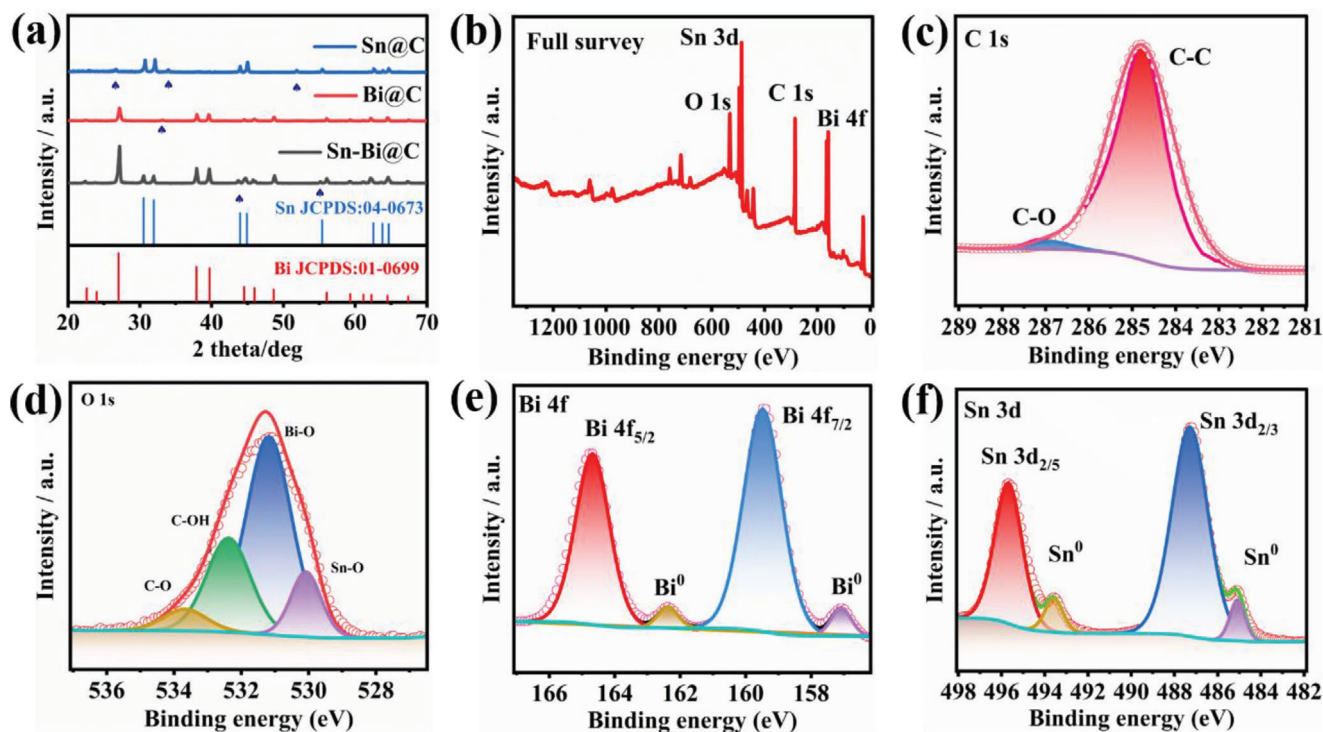


Figure 2. a) XRD patterns of Sn-Bi@C, Sn@C, and Bi@C materials. b) full XPS spectrum, and c–f) high-resolution XPS spectrum of c) C 1s, d) O 1s, e) Bi 4f, and f) Sn 3d for Sn-Bi@C.

and Bi metals (Sn: 231.9 °C; Bi: 271.3 °C). During sintering, the higher-melting Bi stays solid, while the lower-melting Sn melts and forms a liquid phase. This liquid phase spreads over the surface of the solid Bi core, creating stellar nanoparticles.^[17] For comparison, the Sn@C and Bi@C materials are fabricated by similar methods without bismuth and tin sources, respectively. The SEM images of commercial Sn powder, Sn@C and Bi@C show that all of them are random blocky structures (Figure S2a–c, Supporting Information). And the STEM and elemental mapping images of Sn@C and Bi@C demonstrate that Sn and Bi nanoparticles embedded in the carbon matrix (Figure S3a–f, Supporting Information). The selected area electron diffraction patterns are used to prove the crystallinity of Sn-Bi@C, which exhibits characteristics of both Sn@C and Bi@C (Figure S3g–i, Supporting Information).

X-ray diffraction data and Raman spectra provide valuable insights into the structural characteristics of the three samples. **Figure 2a** demonstrates that the Sn-Bi@C composites do not exhibit the presence of alloy formation between the metallic elements Sn and Bi. This absence of alloy formation can be attributed to the thermodynamic immiscibility of the constituent elements.^[17] Additionally, it is evident that all three composites Sn-Bi@C, Sn@C, and Bi@C exhibit excellent correspondence. The peaks marked with blue icons represent the unavoidable oxidation that occurs during calcination, and the standard reference patterns of bismuth oxide and tin dioxide are listed in Figure S3a (Supporting Information). The Raman spectra proved the presence of carbon in Sn-Bi@C, Sn@C, and Bi@C, and the calculated I_D/I_G values for the three samples were 0.97, 0.96, and 1.01, respectively (Figure S4b, Supporting Information). The

higher I_D/I_G value, the more carbon defects, which is conducive to sodium ion storage.^[18–19]

To investigate the elemental composition of the surface of Sn-Bi@C composite, we employed X-ray photoelectron spectroscopy (XPS) for comprehensive characterization analysis. The full XPS spectrum of Sn-Bi@C exhibits that the material is composed of C, O, Sn, and Bi elements, and the states of each element are detailed in the high-resolution spectrum (Figure 2b–f). In the high-resolution spectrum of the C 1s, 284.7 eV belongs to the C–C bond (Figure 2c). The peaks with bonding energies of 533.7, 531.8, and 530.08 eV in the O 1s spectrum are assigned to C–OH, Bi–O, and Sn–O bonds, respectively (Figure 2d). The oxygen-containing functional groups on the carbon surface are a result of the partial oxidation of precursor carbon during calcination.^[20] In the orbital of metallic element Sn 3d, 495.6 and 487.2 eV are belong to the orbital Sn 3d_{2/5} and Sn 3d_{2/3}, respectively, and the valence state is Sn⁴⁺, which is assigned to SnO₂.^[21] While 493.5 and 485.1 eV belong to Sn of zero valence state (Figure 2e). In the orbital of metal element Bi 4f, there are also two valence states of Bi, corresponded to Bi³⁺ in Bi₂O₃ and Bi⁰ (Figure 2f).^[22] Specifically, the peaks at 164.6 and 158.7 eV are attributed to Bi 4f_{5/2}, Bi 4f_{7/2}, respectively, while at 162.4 and 157.1 eV are attributed to Bi⁰. The contents of elements in the three materials are specifically evaluated using the inductively coupled plasma emission spectrometer (ICP) test (Table S1, Supporting Information). For the Sn-Bi@C composite, the content of Bi and Sn elements is 61.081 and 25.320 wt%, respectively. In the Sn-Bi@C composite, the content of Bi element is 61.081 wt%, while the content of Sn element is 25.320 wt%. These weight percentages provide valuable information about the composition and relative amounts of

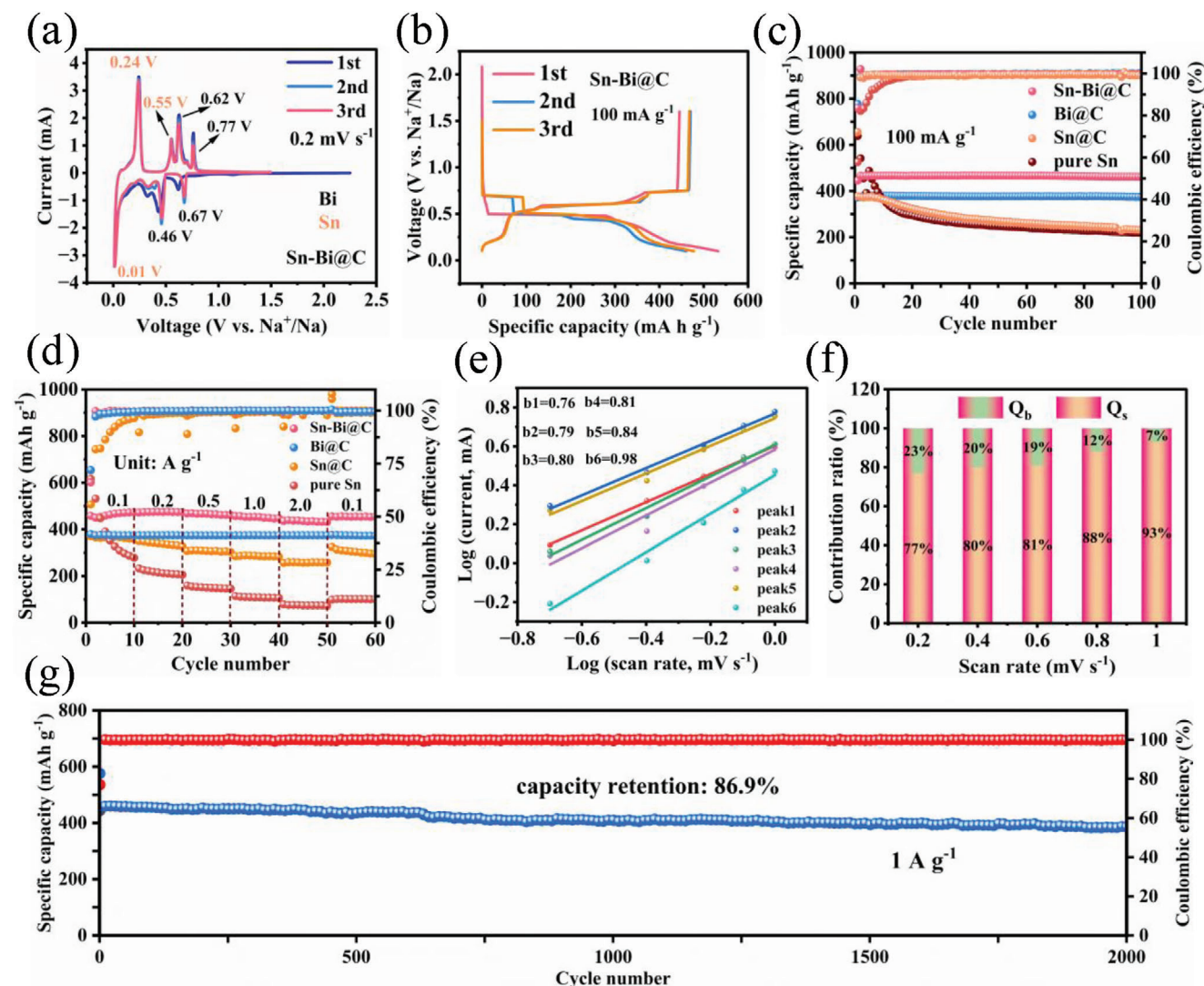


Figure 3. Electrochemical performance of the Sn-Bi@C electrode. a) CV curves at 0.2 mV s^{-1} in the voltage range from 0.1 to 1.5 V. b) Galvanostatic charge/discharge curves at 0.1 A g^{-1} . c) Cycling performances of pure Sn, Sn@C, Bi@C, and Sn-Bi@C electrodes at 100 mA g^{-1} . d) Rate performance at different current densities. e) The fitted linear relationship of $\log(v)$ versus $\log(i)$ for Sn-Bi@C based on the CV curves at different scan rates (0.2, 0.4, 0.8, and 1.0 mV s^{-1} , respectively). f) Contribution ratio of capacitive and diffusion-controlled behaviors at different scan rates in Sn-Bi@C electrode. g) Long-term cycling performance of Sn-Bi@C electrode at 1 A g^{-1} .

Bi and Sn elements in the Sn-Bi@C composite. In Sn@C composite, the content of Sn accounts for 27.38 wt%, and in Bi@C composite, the content of Bi is significantly higher, constituting 80.26 wt% of the composite's composition. Metal bismuth (Bi) is known to exhibit more stable properties compared to metal tin (Sn) as an anode material in sodium ion batteries. The volume expansion rates of these two metals are 244% (Bi) and 420% (Sn), respectively. Given these properties, when bismuth (Bi) content is dominant, it tends to contribute to better material stability.

The electrochemical performance is thoroughly investigated and analyzed. **Figure 3a** displays the initial three cyclic voltammetry (CV) curves of Sn-Bi@C anode at 0.2 mV s^{-1} . The peak at 0.62, 0.77, 0.46, and 0.67 V corresponds to the alloying/dealloying reaction of Bi and Na ($\text{Na}_3\text{Bi} \leftrightarrow \text{Bi}$).^[7] The remaining redox peaks (0.01, 0.24, and 0.55 V) relate to the alloying reaction of Sn and

Na ($\text{Na}_{15}\text{Sn}_4 \leftrightarrow \text{Sn}$).^[23] The CV curves of Sn@C and Bi@C show a typical shape, consistent with previous work (Figure S5a,b, Supporting Information). The first three charge/discharge curves of Sn-Bi@C are displayed in Figure 3b. Compared with the curve characteristics of Sn@C and Bi@C (Figure S5a,b, Supporting Information), it is evident that the platforms associated with the alloying reactions between Bi and Sn with Na are prominently reflected in the Sn-Bi@C curve, indicating that the active involvement of both Bi and Sn in the electrochemical reaction within the Sn-Bi@C electrode. And the initial Coulombic efficiencies of the three materials are 83.6%, 72.5%, and 82.7%, respectively. In Figure 3c, the comparison of cyclic performances of Sn-Bi@C, Sn@C, Bi@C, and pure Sn are tested at 100 mA g^{-1} . Obviously, the Sn-Bi@C electrode exhibits optimal capacity and cyclic stability, delivering a specific capacity of 461 mA h g^{-1} after 100

cycles. In contrast, the capacities of Sn@C, Bi@C, and pure Sn are 374, 232, and 219 mA h g⁻¹ after 100 cycles, with both Sn@C and pure Sn exhibiting noticeable performance attenuation. The corresponding rate performance of Sn-Bi@C, Sn@C, Bi@C, and pure Sn are shown in Figure 3d. At current densities of 0.1, 0.2, 0.5, 1.0, and 2.0 A g⁻¹, the specific capacity of Sn-Bi@C is 458.7, 472.2, 467.9, 456.9, and 436.2 mA h g⁻¹, respectively. While at the current density of 2.0 A g⁻¹, the specific capacities of Sn@C, Bi@C, and pure Sn are significantly lower, measuring only 374.3, 256.7, and 78.9 mA h g⁻¹, respectively.

The CV curve of Sn-Bi@C electrode at different sweep speeds are investigated, and the selected five different sweep speeds are 0.2, 0.4, 0.6, 0.8, and 1.0 mV s⁻¹ (Figure S6, Supporting Information). The character oxidation and reduction peaks are observed at different scanning rates. The intensity of each peak increases with scan rate, while the change in redox peak potential is negligible. This observation suggests that the electrode kinetics are fast and highly reversible. As previously reported, the possible sodium storage mechanism of Sn-Bi@C electrode can be well analyzed by the following formula^[24–26]

$$i = av^b \quad (1)$$

$$\log i = b \log v + \log a \quad (2)$$

where the variable is b , and the slope can be calculated by the $\log i$ - $\log v$ graph. As the parameter "b" approaches 0.5, the behavior of the process is dominated by diffusion (denoted as Q_d). Conversely, as "b" approaches 1, capacitive behavior becomes dominant (denoted as Q_s). As observed in Figure 3e, the values of parameter "b" for the four peaks in both samples are close to 1, indicating that sodium storage process is mainly controlled by capacitance. Figure 3f shows that the Q_s value is calculated to be 77% at 0.2 mV s⁻¹ and gradually increased up to 93% at 1 mV s⁻¹. In the long-term cycle performance test at 1.0 A g⁻¹ (Figure 3g), Sn-Bi@C shows a specific capacity of 385 mA h g⁻¹ after 2000 cycles, with a capacity retention rate of 86.9% compared to its initial charge capacity. This indicates that Sn-Bi@C maintains a significant portion of its initial capacity over multiple cycles. To further elucidate the reasons behind the excellent performance of Sn-Bi@C, further investigations have been undertaken.

The Sn-Bi@C and Sn@C electrodes are subjected to 100 cycles at a current density of 100 mA g⁻¹. After completing the cycling, the batteries are disassembled to investigate the morphologies of the electrodes. As depicted in Figure S8 (Supporting Information), it is obvious that after 100 cycles, the Sn-Bi@C electrode maintains its structural integrity (Figure S8a,S8b, Supporting Information), while the Sn@C electrode display noticeable cracks (Figure S8c,S8d, Supporting Information). We also have performed the TEM image of Sn-Bi@C material after 5 cycles at 0.2 A g⁻¹. As shown in Figure S9 (Supporting Information), the bimetallic nanoparticles retain a well-preserved carbon coating, demonstrating the remarkable cycle stability of Sn-Bi@C. And the corresponding EDX elemental mapping images show the uniform distribution of carbon, bismuth (Bi), tin (Sn), and sodium (Na) elements across the material. This observation further supports the notion that the presence of Bi in Sn-Bi@C composite can alleviate the drastic volume changes that experienced by Sn and maintain structural stability, thereby contributing to

improved cyclic stability. Moreover, for an enhanced comprehension of the structural attributes exhibited by Sn-Bi@C composites, an investigation employing geometric phase analysis (GPA) was conducted utilizing high-resolution TEM imagery.^[27–29] As depicted in Figure 4, the lattice of the bimetallic heterojunction involving Bi and Sn manifests pronounced strains in the e_{xx} and e_{yy} directions. Within this strain profile, the transition from the red to yellow regions corresponds to tensile strain, while the transition from dark blue to light blue signifies compression strain. The stresses arising from these strains effectively mitigate the internal strain induced by sodification, thereby bolstering the structural integrity and augmenting the cyclic performance. From another point of view, we employ the finite element analysis method to simulate the stress experienced by Sn@C and Sn-Bi@C electrodes during sodiation/desodiation process. As Figure 4d,e shown, the Sn@C exhibits significantly higher maximum and minimum stresses (63.7 and 3.92 GPa, respectively) compared to the Sn-Bi@C electrode (31 and 0.336 GPa, respectively). The results suggest that the Sn-Bi@C electrode possesses a superior capacity to buffer the volume expansion in comparison to Sn@C electrode during the charge and discharge process. This discrepancy serves to elucidate the diminished cyclic stability observed in Sn@C electrode.^[30–31]

To elucidate the disparity in electrochemical performance, particularly the enhanced capacity exhibited by Sn-Bi@C compared to Bi@C, we conduct density functional theory (DFT) calculations.^[32] Initially, we analyze the total and partial density of states (TDOS and PDOS) to assess the electronic conductivity, which provided further evidence of the superior electronic conductivity of Sn-Bi@C (Figure 5a) in comparison to Bi@C (Figure 5b).^[33] Subsequently, we investigate the migration pathways of Na ions in both samples and evaluate the associated kinetic energy barriers (Figures S10 and S11, Supporting Information). Remarkably, Sn-Bi@C and Sn@C demonstrate Na adsorption energies of -0.90 and -0.65 eV, respectively, suggesting a more stable adsorption phenomenon in the Sn-Bi@C electrode.^[34] In addition, the Sn-Bi@C (0.30 eV) possesses a lower Na⁺ diffusion energy barrier than Bi@C (0.36 eV) (Figure 5d), indicating more facile Na ion diffusion process in the former material. These findings collectively indicate the superior high-rate performance potential of Sn-Bi@C.^[35] Furthermore, the charge density difference (CDD) and Bader charge of Bi@C and Sn-Bi@C were also calculated and discussed to analyze charge transfer condition. As shown in Figure S12 and Table S2 (Supporting Information), the CDD and Bader charge result demonstrated that Sn is more favorable to the accumulation of electrons at the interface, which is conducive to the enhancement of the batteries performance. The electrochemical impedance spectroscopy diagram of the Sn-Bi@C electrode clearly displays the decreased impedance after cycling (Figure S13, Supporting Information).^[36] The phase transition during charge and discharge of Sn-Bi@C was investigated by ex situ X-ray diffraction (XRD) testing. The results show that the alloying reaction of Bi and Sn is reversible during charge and discharge (Figure S14, Supporting Information).

Considering the exceptional electrochemical performance exhibited by the half-cell, sodium vanadium phosphate (NVP) is selected as the cathode materials to construct a NVP | Sn-Bi@C full cell. Figure S15 (Supporting Information) shows the typical

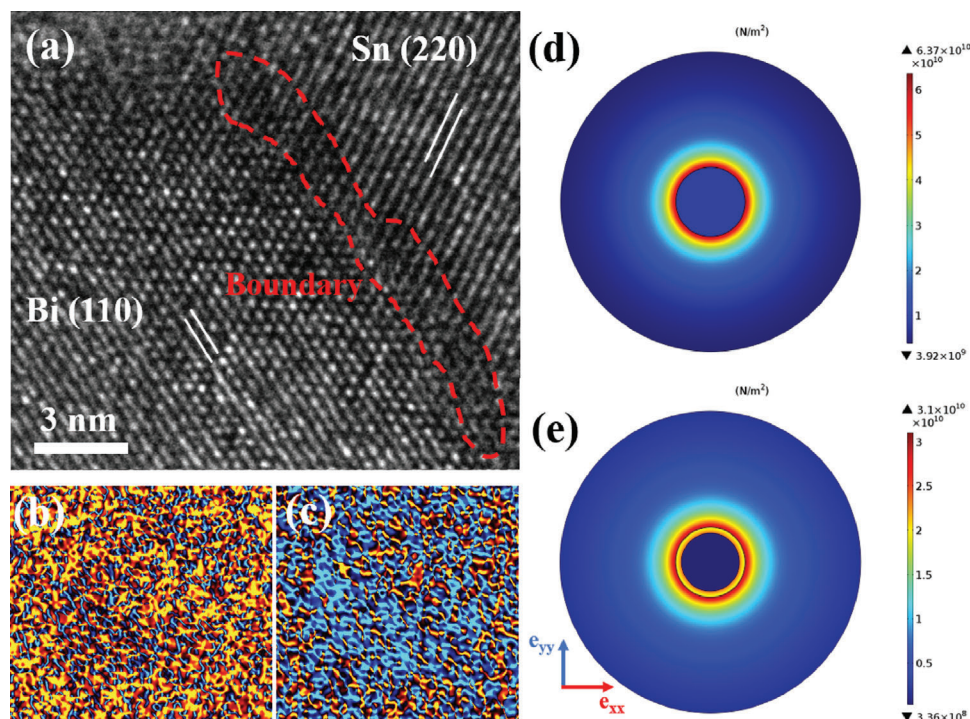


Figure 4. a) HR-TEM image and b–c) strain distribution of b) e_{xx} and c) e_{yy} for Sn-Bi@C, revealing the presence of significant strains. The color scale in the data bar ranges from blue to dark blue, representing compressive strain, while the colors from red to bright yellow indicate tensile strain. d,e) The stress magnitude and distribution of d) Sn@C and e) Sn-Bi@C at the state of complete sodiation analyzed by finite element simulation.

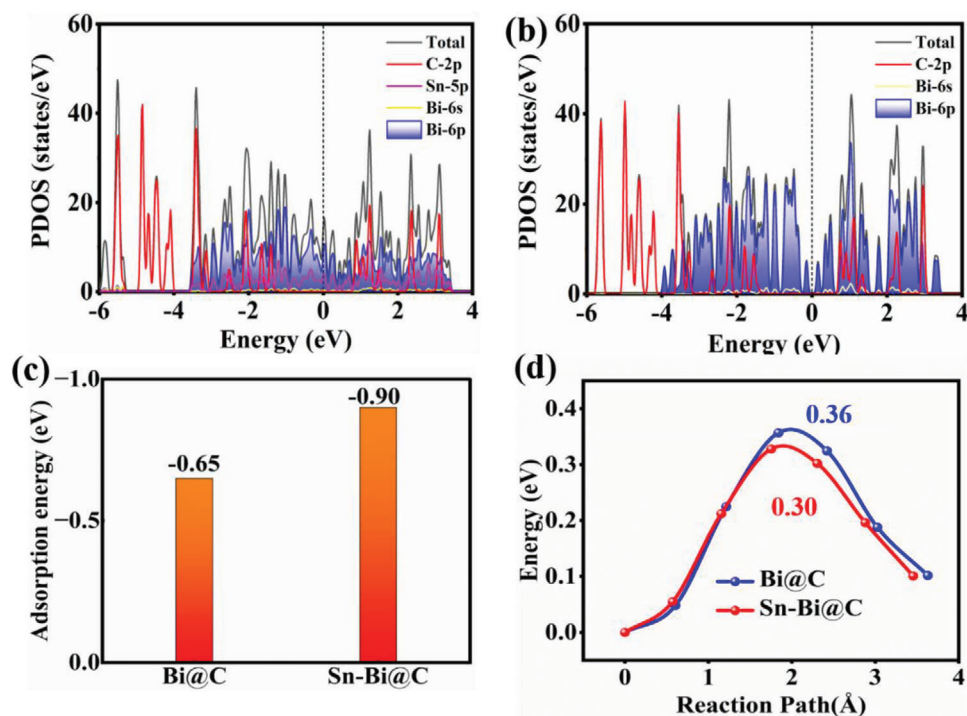


Figure 5. Theoretical calculation based on DFT. Calculated PDOS of a) Sn-Bi@C and b) Bi@C. c) Comparison of Na adsorption energy and d) Na diffusion energy barriers in Sn-Bi@C and Bi@C.

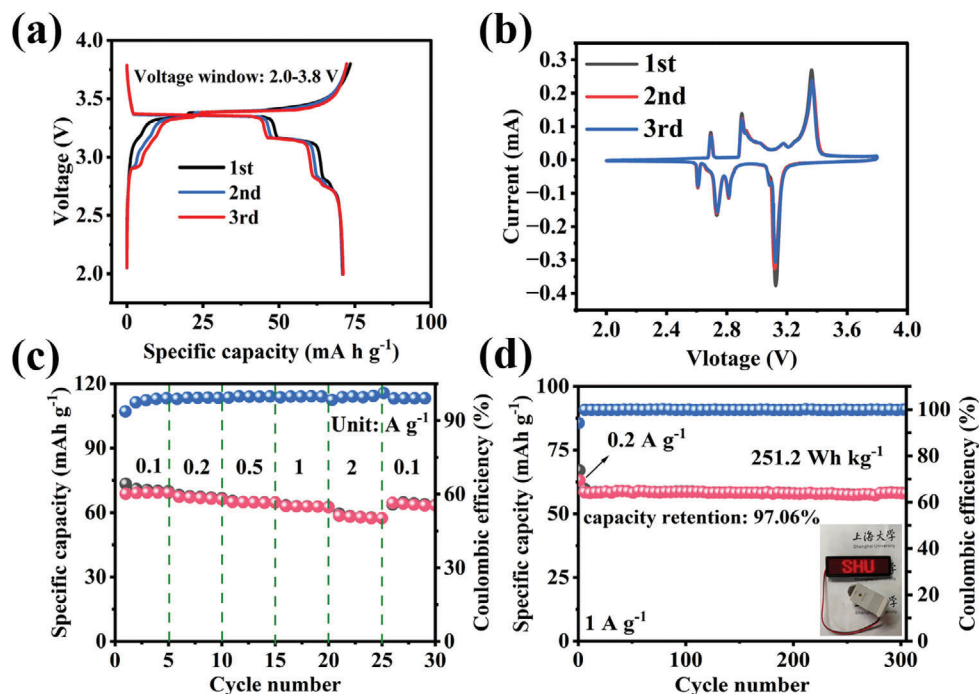


Figure 6. Electrochemical performance of NVP | Bi@MC full cells. a) Typical charge/discharge curves of the NVP cathode. b) CV curves at 0.1 mV s^{-1} . c) Rate performance. d) Cycling performance at 1 A g^{-1} .

CV curve of NVP. The NVP is a renowned cathode material in the field of sodium-ion batteries, owing to its exceptional characteristics including high specific capacity, excellent rate performance, and prolonged cycle life.^[37–40] As illustrated in **Figure 6a**, the initial three charge/discharge curves of NVP | Sn-Bi@C full cell demonstrate remarkable concurrence, indicating a high degree of the electrochemical reversibility. This observation is further supported by the CV curves of the 1st, 2nd, and 3rd cycles presented in **Figure 6b**, which exhibit consistency with the charge/discharge results, underscoring the highly reversible nature of the electrochemical reaction. Notably, the platform positions behave a minor deviation with the published work.^[41] This discrepancy is primarily attributed to differences in the charge and discharge cut-off voltages.^[42] During the rate performance evaluation of the full cell, specific capacities of 73.4, 67.3, 64.9, 62.9, and 58.5 mA h g^{-1} were achieved at current densities of 0.1, 0.2, 0.5, 1.0, and 2.0 A g^{-1} , respectively (**Figure 6c**). Remarkably, the long-term cyclic stability of the NVP | Sn-Bi@C full cell is exceptionally robust, as evidenced by a capacity retention of 97.02% after 300 cycles at 1 A g^{-1} (**Figure 6d**). Based on the total mass of the anode and cathode active materials, the NVP | Sn-Bi@C full cell exhibits a high energy density up to $251.2 \text{ W h kg}^{-1}$. Moreover, a practical application test on the full cell was conducted, successfully illuminating an LED lamp (inset in **Figure 6d**).

3. Conclusion

In summary, a special designed Sn-Bi@C stellar nanoparticles with Bi-core encapsulated into the Sn envelop have been successfully fabricated via a facile annealing strategy. The com-

posed influence of the encased Bi and enveloped Sn manifests a uniform stress distribution within the Sn-enveloped Bi structure, effectively mitigating the structural strain induced by the Na^+ ion insertion process. Simultaneously, the bimetallic nature of the stellar nanosphere enhances electrical conductivity and promotes accelerated diffusion kinetics of sodium ions. As a result of these unique structural advantages, the Sn-Bi@C anode delivers superior electrochemical performance for SIBs. It achieves remarkable specific capacity of 461 mA h g^{-1} after 100 cycles at 100 mA g^{-1} and maintains 86.9% capacity retention after 2000 cycles at 1 A g^{-1} . Even at a higher current density of 2 A g^{-1} , the capacity remains as high as 436 mA h g^{-1} . Moreover, when integrated into a full cell configuration with $\text{Na}_3\text{V}_2(\text{PO}_4)_3$ cathode, the $\text{Na}_3\text{V}_2(\text{PO}_4)_3$ |Sn-Bi@C full cell demonstrates a high energy density of $251.2 \text{ W h kg}^{-1}$ and stable cycling performance, retaining 97.06% capacity after 300 cycles at 1 A g^{-1} . This research presents a novel concept for the development of bimetallic alloy anodes in sodium-ion batteries, offering promising prospects for their practical applications.

4. Experimental Section

Synthesis of the Sn-Bi@C Composite: 2 mmol $\text{Bi}(\text{NO}_3)_3 \cdot 5\text{H}_2\text{O}$, 2 mmol Sn powder, and 2 mmol $\text{C}_6\text{H}_{12}\text{O}_6$ were dissolved in 30 mL glycol, stirred evenly, and hydrothermal reaction was conducted at 180°C for 12 h. After completion, the powder solids were collected, cleaned to neutral with anhydrous ethanol and deionized water, dried in a vacuum oven at 70°C , and finally kept at 800°C for 2 h in a tubular furnace filled with argon gas.

Synthesis of the Sn@C Composite: 2 mmol Sn powder and 2 mmol $\text{C}_6\text{H}_{12}\text{O}_6$ were dissolved in 30 mL glycol, stirred evenly, and hydrothermal

reaction was conducted at 180 °C for 12 h. After completion, the powder solids were collected, cleaned to neutral with anhydrous ethanol and deionized water, dried in a vacuum oven at 70 °C, and finally kept at 800 °C for 2 h in a tubular furnace filled with argon gas.

Synthesis of the Bi@C Composite: 2 mmol $\text{Bi}(\text{NO}_3)_3 \cdot 5\text{H}_2\text{O}$ and 2 mmol $\text{C}_6\text{H}_{12}\text{O}_6$ were dissolved in 30 mL glycol, stirred evenly, and hydrothermal reaction was conducted at 180 °C for 12 h. After completion, the powder solids were collected, cleaned to neutral with anhydrous ethanol and deionized water, dried in a vacuum oven at 70 °C, and finally kept at 800 °C for 2 h in a tubular furnace filled with argon gas.

Material Characterization: The structure details and morphology were collected by electron microscope of Germany ZEISS Gemini-SEM 300 (accelerating voltage = 15 kV) and transmission electron microscope at high-resolution (HR-TEM, JEOL-2100F, accelerating voltage = 200 kV), respectively. The ESCALAB 250Xi was used for XPS analysis. XRD (Rigaku D/MAX 2200 V) patterns were achieved via Cu K α radiation in the range from 10° to 90° (2 θ) at 8° min⁻¹ of scanning rate. The detailed procedure of in situ XRD was described in the Supporting Information. N₂ adsorption-desorption analysis was performed on a Micro-meritics ASAP 2460 instrument (Micromeritics, Norcross, GA). The pore size distribution of the as-prepared samples was obtained through the method of Barrett Joyner Halenda (BJH).

Electrochemical Section: The electrochemical properties of three samples were tested by applying standard CR-2032-coin batteries prepared in a glove box filled with Ar ($\text{H}_2\text{O} < 10^{-2}$ ppm, $\text{O}_2 < 10^{-2}$ ppm). For half cells, the Bi@MC electrode materials, conductive carbon, and polyvinylidene fluoride (PVDF) binder were uniformly mixed in an 8:1:1 weight ratio, dispersed in *N*-Methylpyrrolidone (NMP) to make an electrode slurry, and then was coated onto the copper foil and vacuum dried at 120 °C overnight. The areal mass loadings of the Bi@MC on the copper foil were about 1.0–1.5 mg cm⁻². For the assembly of half cells, the separator is glass fiber, pure Na metal as the counter electrode, and 100 μL electrolyte was used per coin cell, which was prepared by dissolving hexafluorophosphate (NaPF_6) in ethylene glycol dimethyl ether (DME). The CHI 660D workstation is used to test the cyclic voltammetry (CV) at 0.1 mV s⁻¹ from 0.1 to 1.5 V versus Na⁺/Na. Constant current charge/discharge measurements of Na⁺/Na were performed at room temperature with a voltage range from 0.1 to 1.5 V, using the Neware battery test system. CHI 660D workstation provided the measurements of impedance spectra of electrochemical with the frequency range from 100 kHz to 0.01 Hz. For full cell, using commercial $\text{Na}_3\text{V}_2(\text{PO}_4)_3$ (NVP, Guandong Canrd New Energy Technology Co., Ltd) as a cathode. NVP powder was mixed with conductive carbon and PVDF in a 7:2:1 weight ratio and dispersed in NMP to make an electrode slurry, and then the mixed slurry was coated onto the aluminum foil and vacuum dried at 120 °C overnight. The NVP cathode and Bi@MC anode were partnered in a weight ratio of 1:4 in 2032-type coin cells with NaPF_6 + DME (100 μL) as electrolyte. Specially, the anode (Bi@MC) pretreated charged/discharged with 5 cycles before assembling full cells.

Calculation Method: First-principle calculations were performed by the DFT using the Vienna Ab-initio Simulation Package (VASP) package.^[43] The generalized gradient approximation with the Perdew–Burke–Ernzerhof functional was used to describe the electronic exchange and correlation effects.^[44–46] Uniform G-centered k-points meshes with a resolution of $2\pi \times 0.04 \text{ \AA}^{-1}$ and Methfessel–Paxton electronic smearing were adopted for the integration in the Brillouin zone for geometric optimization. The simulation was run with a cutoff energy of 500 eV throughout the computations. These settings ensure convergence of the total energies to within 10 meV per atom. Structure relaxation proceeded until all forces on atoms were less than 10 meV \AA^{-1} and the total stress tensor was within 0.03 GPa of the target value. The transition state energy barriers were estimated using the nudged elastic band method.^[47,48]

Supporting Information

Supporting Information is available from the Wiley Online Library or from the author.

Acknowledgements

J.C. and G.Z. contributed equally to this work. This project was financially supported by the Australian Research Council (ARC) through the ARC Future Fellowship (No. FT180100705). H.G. thanked the support from Open Project of State Key Laboratory of Advanced Special Steel, the Shanghai Key Laboratory of Advanced Ferrometallurgy, Shanghai University (No. SKLASS 2021-04), the Science and Technology Commission of Shanghai Municipality (No. 22010500400), “Joint International Laboratory on Environmental and Energy Frontier Materials” and “Innovation Research Team of High-Level Local Universities in Shanghai” in Shanghai University.

Open access publishing facilitated by University of Technology Sydney, as part of the Wiley - University of Technology Sydney agreement via the Council of Australian University Librarians.

Conflict of Interest

The authors declare no conflict of interest.

Data Availability Statement

The data that support the findings of this study are available in the Supporting Information of this article.

Keywords

bimetallic materials, homogeneous stress distribution, sodium-ion batteries, stellar configuration

Received: July 11, 2023

Revised: September 6, 2023

Published online: September 17, 2023

- [1] D. Hou, D. Xia, E. Gabriel, J. A. Russell, K. Graff, Y. Ren, C.-J. Sun, F. Lin, Y. Liu, H. Xiong, *ACS Energy Lett.* **2021**, *6*, 4023.
- [2] A. Rudola, R. Sayers, C. J. Wright, J. Barker, *Nat. Energy* **2023**, *8*, 215.
- [3] G. Li, S. Guo, B. Xiang, S. Mei, Y. Zheng, X. Zhang, B. Gao, P. K. Chu, K. Huo, *Energy Mater.* **2022**, *2*, 200020.
- [4] H. Liu, X. Liu, W. Li, X. Guo, Y. Wang, G. Wang, D. Zhao, *Adv. Energy Mater.* **2017**, *7*, 1700283.
- [5] D. Yan, Y. V. Lim, G. Wang, Y. Shang, X. L. Li, D. Fang, M. E. Pam, S. A. Yang, Y. Wang, Y. Shi, H. Y. Yang, *ACS Nano* **2021**, *15*, 8507.
- [6] W. Zhao, X. Ma, Y. Zheng, L. Yue, C. Xu, G. Wang, Y. Luo, D. Zheng, S. Sun, A. A. Alshehri, X. Sun, C. Tang, *Chem. Eng. J.* **2023**, *459*, 141629.
- [7] W. Hong, A. Wang, L. Li, T. Qiu, J. Li, Y. Jiang, G. Zou, H. Peng, H. Hou, X. Ji, *Adv. Funct. Mater.* **2021**, *31*, 2000756.
- [8] Y. Xiang, L. Xu, L. Yang, Y. Ye, Z. Ge, J. Wu, W. Deng, G. Zou, H. Hou, X. Ji, *Nano-Micro Lett.* **2022**, *14*, 136.
- [9] C. C. Wang, L. B. Wang, F. J. Li, F. Y. Cheng, J. Chen, *Adv. Mater.* **2017**, *29*, 7.
- [10] Y. Liang, N. Song, Z. Zhang, W. Chen, J. Feng, B. Xi, S. Xiong, *Adv. Mater.* **2022**, *34*, 2202673.
- [11] S. Guo, H. Li, Y. Lu, Z. Liu, X. Hu, *Energy Storage Mater.* **2020**, *27*, 270.
- [12] J. Zhao, J. Xu, Q. Li, W. Yao, C. Yu, N. Zhang, X. Chen, X. Ding, J. *Electroanal. Chem.* **2023**, *939*, 117452.
- [13] J. Chen, J. Xiao, J. Li, H. Gao, X. Guo, H. Liu, G. Wang, *J. Mater. Chem. A* **2022**, *10*, 20635.
- [14] C. Zheng, D. Ji, Q. Yao, Z. Bai, Y. Zhu, C. Nie, D. Liu, N. Wang, J. Yang, S. Dou, *Angew. Chem., Int. Ed.* **2023**, *62*, 202214258.
- [15] J. Yang, X. Guo, H. Gao, T. Wang, Z. Liu, Q. Yang, H. Yao, J. Li, C. Wang, G. Wang, *Adv. Energy Mater.* **2023**, *13*, 2300351.

- [16] Y. H. Kim, J. H. An, X. Li, J. Y. Moon, H. Yu, H. J. Ahn, J. C. Lee, *Adv. Funct. Mater.* **2023**, *16*, 2301552.
- [17] C. Yang, B. H. Ko, S. Hwang, Z. Liu, Y. Yao, W. Luc, M. Cui, A. S. Malkani, T. Li, X. Wang, J. Dai, B. Xu, G. Wang, D. Su, F. Jiao, L. Hu, *Sci. Adv.* **2020**, *6*, eaaz6844.
- [18] J. Huo, X. Cao, Y. Tian, L. Li, J. Qu, Y. Xie, X. Nie, Y. Zhao, J. Zhang, H. Liu, *Nanoscale* **2023**, *15*, 5448.
- [19] X. Yao, Y. Ke, W. Ren, X. Wang, F. Xiong, W. Yang, M. Qin, Q. Li, L. Mai, *Adv. Energy Mater.* **2019**, *9*, 1803260.
- [20] T. Xu, X. Qiu, X. Zhang, Y. Xia, *Chem. Eng. J.* **2023**, *452*, 139514.
- [21] W. Luc, C. Collins, S. Wang, H. Xin, K. He, Y. Kang, F. Jiao, *J. Am. Chem. Soc.* **2017**, *139*, 1885.
- [22] J. X. Qiu, S. Li, X. T. Su, Y. Z. Wang, L. Xu, S. Q. Yuan, H. M. Li, S. Q. Zhang, *Chem. Eng. J.* **2017**, *320*, 300.
- [23] Y. Zhu, Z. Qian, J. Song, W. Du, J. Pan, D. Wang, J. Yang, *Nano Lett.* **2021**, *21*, 3588.
- [24] A. Schoedel, Z. Ji, O. M. Yaghi, *Nat. Energy* **2016**, *1*, 16034.
- [25] L. M. Zhou, K. Zhang, J. Z. Sheng, Q. Y. An, Z. L. Tao, Y. M. Kang, J. Chen, L. Q. Mai, *Nano Energy* **2017**, *35*, 281.
- [26] G. A. Muller, J. B. Cook, H. S. Kim, S. H. Tolbert, B. Dunn, *Nano Lett.* **2015**, *15*, 1911.
- [27] M. J. Hÿtch, E. Snoeck, R. Kilaas, *Ultramicroscopy* **1998**, *74*, 131.
- [28] J. Hao, Z. Zhuang, J. Hao, K. Cao, Y. Hu, W. Wu, S. Lu, C. Wang, N. Zhang, D. Wang, M. Du, H. Zhu, *ACS Nano* **2022**, *16*, 3251.
- [29] Z. Du, C. Wu, Y. Chen, Z. Cao, R. Hu, Y. Zhang, J. Gu, Y. Cui, H. Chen, Y. Shi, J. Shang, B. Li, S. Yang, *Adv. Mater.* **2021**, *33*, 2101473.
- [30] H. Yu, Y. Cao, L. Chen, Y. Hu, X. Duan, S. Dai, C. Li, H. Jiang, *Nat. Commun.* **2021**, *12*, 4564.
- [31] S. Zhang, F. Ling, L. Wang, R. Xu, M. Ma, X. Cheng, R. Bai, Y. Shao, H. Huang, D. Li, Y. Jiang, X. Rui, J. Bai, Y. Yao, Y. Yu, *Adv. Mater.* **2022**, *34*, 2201420.
- [32] X. Li, X. Zhang, X. Niu, J. Zhang, R. Wu, J. S. Chen, Y. Yu, *Adv. Funct. Mater.* **2023**, *33*, 2300914.
- [33] H. Li, Y. Li, L. Zhang, *SusMat* **2022**, *2*, 34.
- [34] J. Liu, S. Xiao, X. Li, Z. Li, X. Li, W. Zhang, Y. Xiang, X. Niu, J. S. Chen, *Chem. Eng. J.* **2021**, *417*, 129279.
- [35] S. Xiao, Z. Li, J. Liu, Y. Song, T. Li, Y. Xiang, J. S. Chen, Q. Yan, *Small* **2020**, *16*, 2002486.
- [36] L. Chen, X. He, H. Chen, S. Huang, M. Wei, *J. Mater. Chem. A* **2021**, *9*, 22048.
- [37] G. Chen, Q. Huang, T. Wu, L. Lu, *Adv. Funct. Mater.* **2020**, *30*, 2001289.
- [38] Y. Liu, X. Wu, A. Moez, Z. Peng, Y. Xia, D. Zhao, J. Liu, W. Li, *Adv. Energy Mater.* **2023**, *13*, 2203283.
- [39] W. Zhang, Y. Wu, Z. Xu, H. Li, M. Xu, J. Li, Y. Dai, W. Zong, R. Chen, L. He, Z. Zhang, D. J. L. Brett, G. He, Y. Lai, I. P. Parkin, *Adv. Energy Mater.* **2022**, *12*, 2201065.
- [40] T. Jin, X. Ji, P.-F. Wang, K. Zhu, J. Zhang, L. Cao, L. Chen, C. Cui, T. Deng, S. Liu, N. Piao, Y. Liu, C. Shen, K. Xie, L. Jiao, C. Wang, *Angew. Chem., Int. Ed.* **2021**, *60*, 11943.
- [41] M. H. Cao, Z. Shadik, S.-M. Bak, T. Wang, E. Hu, S. Ehrlich, Y. N. Zhou, X. Q. Yang, Z. W. Fu, *Energy Storage Mater.* **2020**, *24*, 417.
- [42] X. Hou, Y. Zhu, Q. Yao, J. Song, C. Wang, Y. Zhou, S. Zeng, J. Yang, Y. Qian, *J. Energy Chem.* **2023**, *79*, 468.
- [43] G. Kresse, J. Furthmüller, *Comput. Mater. Sci.* **1996**, *6*, 15.
- [44] J. P. Perdew, K. Burke, M. Ernzerhof, *Phys. Rev. Lett.* **1996**, *77*, 3865.
- [45] P. E. Blöchl, *Phys. Rev. B: Condens. Matter Mater. Phys.* **1994**, *50*, 17953.
- [46] G. Kresse, D. Joubert, *Phys. Rev. B: Condens. Matter Mater. Phys.* **1999**, *59*, 1758.
- [47] G. Henkelman, H. Jonsson, *J. Chem. Phys.* **2020**, *113*, 9978.
- [48] B. Kaduk, T. Kowalczyk, T. Van Voorhis, *Chem. Rev.* **2012**, *112*, 321.